Cross sections for the three-body photodisintegration of ^{3}He at $E_\gamma = 12.8$, 13.5, and 14.7 MeV

B. A. Perdue,[*] M. W. Ahmed, S. S. Henshaw, P.-N. Seo,[†] S. Stave,[‡] and H. R. Weller
Triangle Universities Nuclear Laboratory, Duke University, P. O. Box 90308, Durham, North Carolina 27708-0308, USA

P. P. Martel and A. Teymurazyan
Department of Physics, University of Massachusetts, Amherst, Massachusetts 01003, USA
(Received 31 December 2010; published 10 March 2011)

The absolute differential cross sections for the ^{3}He(γ,n)pp reaction were measured as a function of outgoing neutron scattering angle and energy at the incident γ-ray energies of 12.8, 13.5, and 14.7 MeV to within a precision better than $\pm$6%. Both the absolute cross sections and the neutron energy distributions at each incident γ-ray energy agree with the state-of-the-art theoretical results when the Coulomb interaction in the final state is included.

DOI: 10.1103/PhysRevC.83.034003 PACS number(s): 25.10.+s, 25.20.Dc, 21.60.De, 29.40.Mc

I. INTRODUCTION

Interest in the photoeffect on trinucleon systems began in the early sixties with the first significant experiments [1] on the photodisintegration of ^{3}He and has continued to the present day. Much of the work during the 1960s, 1970s, and 1980s centered around measurements [2] and calculations [3] of the three-body (the two-body channel was also studied) total cross sections as a function of the incident γ-ray energy. Through the interplay of theory and experiment in these earlier works, it was discovered that nuclear interactions between pairs of nucleons in the final state dominated the reaction cross section. Although these earlier measurements were paramount in guiding the theoretical efforts, there still exists disagreement between some of the results at lower γ-ray energies (below 16 MeV) [2,4].

More recent measurements of the total three-body photodisintegration cross section were performed by Naito *et al.* [4] at $E_\gamma = 10.2$ and 16.0 MeV. Their result at 10.2 MeV disagrees with most of the world's data and is below the current theoretical predictions (the calculations were performed by the Krakow-Bochum collaboration) by a factor of about 3.

As we have stated above, much of the previous work performed on the three-body photodisintegration of ^{3}He was directed at measurements of the total cross sections. Very few publications have presented results on the differential aspects of the three-body photodisintegration cross sections at γ-ray energies below 16 MeV. Virtually, the only published results on the neutron angular and energy distributions for the three-body photodisintegration of ^{3}He at low γ-ray energies are those reported by Gorbunov [2]. The data cover a large range in incident γ-ray energy; however, limited statistics forced the author to average the data over γ-ray energy bins of 4 MeV or larger and to integrate over all scattering angles or all neutron energies. Even with averaging over the wide γ-ray energy bins, the resulting statistical error bars for the data below $E_\gamma =$ 16 MeV are on the order of 20% at best. The neutron energy distributions integrated over the scattering angle and averaged over the γ-ray energies of 8 to 12 MeV are shown by Gorbunov to be consistent with a phase-space-only neutron energy distribution. In contrast to the lower energy data, the neutron energy distribution averaged over the 12–16 MeV bin shows a pronounced peak at $\approx 0.85 \times E_n^{\max}$, where $E_n^{\max}$ is the maximum neutron energy allowed by the kinematics of the reaction. The enhancement at the higher neutron energies in this distribution was shown to be due to the pp nuclear final-state interaction (FSI) by Barbour and Phillips [3]. As a result, the neutron energy distributions at lower γ-ray energies ($E_\gamma = 8$–16 MeV) reported by Gorbunov [2] suggest a sharp transition around $E_\gamma = 12$ MeV from a phase-space-only distribution to a distribution that is dominated by nucleon-nucleon final-state interactions. In addition to confirming the pp FSIs in the reaction, Gibson and Lehman [3] point out (by using an approximation) that Coulomb effects must be included to describe the distribution more accurately.

The inclusion of the Coulomb interaction in the three-body problem has been a long-standing challenge in theoretical nuclear physics. Deltuva, Fonseca, and Sauer [5] have developed a calculational method that allows the use of realistic NN potentials along with the full treatment of the Coulomb interaction in calculations of observables (e.g., neutron energy distributions).

In this paper, we present measurements of the ^{3}He(γ,n)pp reaction at the incident γ-ray energies of $E_\gamma = 12.8$, 13.5, and 14.7 MeV performed at the High Intensity γ-ray Source (HIγS) [6]. We compare our experimental results for the absolute differential three-body cross sections to the state-of-the-art calculations of Deltuva, Fonseca, and Sauer [7] in Sec. IV. The agreement is found to be very good. For completeness, we also compare our results to a calculation where the neutron energy distribution at each scattering angle is determined by phase space alone.

II. DESCRIPTION OF THE EXPERIMENT

A. General

A collimated, pulsed beam of γ rays, produced by the Compton backscattering of free-electron laser (FEL) photons

[*]Now at Los Alamos National Laboratory; perdue@tunl.duke.edu
[†]Now at University of Virginia and TUNL.
[‡]Now at Pacific Northwest National Laboratory.

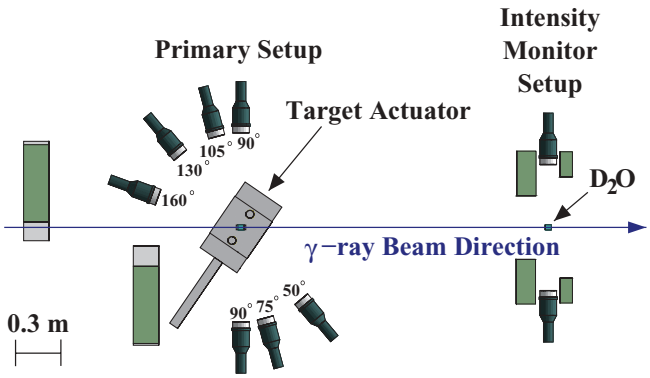

FIG. 1. (Color online) A schematic of the experimental arrangement. The main components are labeled in the figure (D_2O denotes the ^2H_2O target). The target actuator was used to cycle through the main ^{3}He target, the empty target cell, and other targets (as described in the text). The blocks upstream of the primary detectors are lead shielding walls (shown in green online) supported underneath by concrete blocks. The blocks located on either side of the beam intensity monitor detectors (shown in green online) are shielding walls made of lead.

from highly relativistic electrons in the Duke storage ring, were incident on a high-pressure ^{3}He gas target. The outgoing neutrons resulting from the $^3\mathrm{He}(\gamma,n)pp$ reaction were detected in an array consisting of seven liquid scintillator neutron detectors. A simultaneous measurement of the $^2\mathrm{H}(\gamma,n)^1\mathrm{H}$ reaction using two additional liquid scintillator neutron detectors located 2.4 meters downstream of the ^{3}He target was performed to monitor the γ-ray beam intensity and to provide an absolute normalization [using known values of the $^2\mathrm{H}(\gamma,n)^1\mathrm{H}$ cross section] for the ^{3}He photodisintegration measurements.

Figure 1 shows a schematic of the full experimental setup including the primary detector array, beam intensity monitor, and shielding walls. The γ-ray beam was incident from the left as indicated in the figure. A target actuator was utilized to cycle the primary ^{3}He gas target, an empty target cell used for background subtraction, and other targets into the γ-ray beam. We describe the various targets in Sec. II D.

B. γ-ray beam and collimators

The γ-ray beams utilized during the experiments were collimated by two 25.4-mm-diameter lead collimators that were 15.2 cm long. With these collimators in place, beam energy spreads of $\Delta E_\gamma/E_\gamma \approx 5\%$–$6\%$ and beam intensities of 2–7 $\times 10^7$ γ/sec on target were achieved. Pulsed beams of γ rays were generated by scattering FEL photons from two electron bunches circulating inside the electron storage ring. The revolution frequency of a single electron bunch in the storage ring is 2.79 MHz, producing a collision between the electrons and FEL photons every 179 ns (with two electron bunches stored one-half of the circumference apart in the ring). Exploiting the pulsed structure of the beams at HIγS allowed time-of-flight (TOF) methods to be employed to measure the energy of the detected neutrons and to reduce backgrounds that were unrelated to the timing of the beam bursts.

C. Neutron detectors

Nine neutron detectors were used in the experiment described in this paper, where seven detectors comprised the primary array and the two remaining detectors were placed in a separate setup that was used to monitor the γ-ray beam intensity. We describe the beam intensity monitor in Sec. II F. Each of the neutron detectors is a cell filled with BC-501A organic scintillating liquid coupled to a photomultiplier tube. The active volume of each cell has a diameter of 12.7 cm and a length of 5.1 cm. The seven primary detectors were placed at the angles of 50°, 75°, 90° (beam right), 90° (beam left), 105°, 130°, and 160° relative to the γ-ray beam direction. The detector at 160° was placed at a distance of 70 cm from the target center, and all the other detectors were placed at 75 cm from the target center.

D. ^{3}He target and other targets

The primary target for the experiment was a 0.4-L (water) capacity cylindrical bottle filled with 170 bar of ^{3}He gas. The pressurized gas inside the bottle was 99.87% ^{3}He, with the total helium content being greater than 99.999% [8]. The bottle was 22.7 cm in length with a 6.5-cm outer diameter. The walls of the container were 0.5-cm thick. The cylinder was made of aluminum alloy 6082. A second aluminum bottle containing only air at atmospheric pressure that was identical to the primary target bottle was placed in the beam periodically. Runs were taken with the ^{3}He target in place relative to the background target in place with a 2:1 ratio. The data acquired with the background target in the beam were used in the background subtraction step of the analysis (see Sec. III D).

Two additional targets were used in the experiment for diagnostics, systematic checks, and assistance in performing the TDC (time-to-digital converter) to TOF calibrations.

The first target used was a 12.7-cm-diameter aluminum rod. This rod served as a source of Compton-scattered γ rays located at the target center position. The aluminum rod was mounted on the target actuator between the two aluminum target bottles during most of the experiment, and short runs ($\sim$1 min) were executed with it in the beam between each production run. The γ-ray peaks appearing in the TDC spectra from this target (referred to as "γ-flash peaks") were used to track any timing shifts in the TDC spectra. In addition, the centroid location of the γ-flash peaks were used to find the zero points of the TOF spectra by exploiting the fact that it takes a γ ray d/c nanoseconds, where d is the flight path in cm and c is the speed of light in cm/ns, to travel from the target center to the detectors.

The second additional target used in the experiment was a 4.74-cm-long, 4.08-cm-diameter polyethylene cylinder with a wall thickness of 0.7 mm containing heavy water. This ^2H_2O target was placed at the center of the detector array at each γ-ray energy to produce neutrons from the photodisintegration of the deuteron. Since $^2\mathrm{H}(\gamma,n)^1\mathrm{H}$ is a two-body reaction, the outgoing neutrons are monoenergetic. The neutron energy, and thus the time of flight, can be calculated from the reaction kinematics at each scattering angle being measured. This information aided in the calibration of the TDC.

E. Backgrounds

The neutron detectors used in the experiment are sensitive to both neutrons and γ rays. By exploiting the pulse-shape discrimination (PSD) properties of the liquid scintillators, γ-ray events were easily identified and discarded in the analysis, which virtually eliminates any γ-ray background. We describe the PSD event-selection cut in Sec. III C.

There were two primary sources of neutron background: (1) (γ,n) reactions on elements contained in the walls of the aluminum alloy 6082 target bottle and (2) neutrons that were scattered into the detectors that were not initially directed toward a detector (referred to as *in-scattering*). The neutron contribution coming from the walls of the target bottle was investigated by collecting data on the second bottle, which was identical to the primary target bottle and contained only air at atmospheric pressure. The background data collected with the air bottle in the beam were used in the background subtraction portion of the analysis (see Sec. III D). Investigations into the in-scattering and out-scattering contributions were carried out via Monte Carlo simulations, which are described in Sec. III F. The out-scattering of neutrons was purely an attenuation effect. For a given detector, the number of neutrons out-scattered away from their path to intersect the active volume of the detector as given by the results of the simulations was found to be consistent with an attenuation calculation using the known thickness of the walls of the aluminum target bottle.

F. Beam intensity monitoring

A target and detector system was constructed in the rear of the target room to monitor the γ-ray beam intensity via the $^2\mathrm{H}(\gamma,n)^1\mathrm{H}$ reaction. The target was a $^2\mathrm{H}_2\mathrm{O}$ target identical to the one used periodically in the primary setup. The target was a 4.74-cm-long, 4.08-cm-diameter polyethylene cylinder with a 0.7-mm wall thickness filled with heavy water. Two Bicron neutron detectors were placed 50 cm from the target center at 90° on either side of the target. Shielding walls were built on the upstream and downstream sides of the detectors to shield them from scattered γ rays. The beam intensity monitor system is shown on the right side of Fig. 1.

The total cross section of the $^2\mathrm{H}(\gamma,n)^1\mathrm{H}$ reaction has been measured to a precision of 2%–3% in the energy range of the current experiment [9]. The previously measured values of the total cross section were used to extract the γ-ray beam intensity from the 90° yields by assuming that the angular distribution of the neutrons can be written as $A + B\sin^2\theta_n^{\mathrm{cm}}$. The values of A, which are small, and B were chosen based on previous calculations [10] and measurements [11].

III. DATA REDUCTION AND SIMULATIONS

A. General

The experimental data were analyzed to determine absolute cross sections. During the experiment, the data were collected and stored in event mode. The correlation between the parameters of each event were preserved in the event-mode data storage, allowing each event to be reconstructed in the *offline* analysis. Each recorded event possessed an ADC value corresponding to the pulse height (PH) of the event and a pulse-shape discrimination value used for particle identification and discrimination. In addition, each event contained a TDC value corresponding to the time-of-flight value of the particle detected.

Experimental systematic effects such as the finite geometry of the targets and detectors, neutron multiple scattering, and detection efficiencies played a role in the experiment and the determination of the absolute cross sections. These effects and others were investigated through the use of the GEANT4 simulation toolkit [12]. The GEANT4 toolkit was used to model the target room environment and the transport of particles through this environment. The simulations constructed using GEANT4 served to facilitate data analysis and aid in the interpretation of the final results.

B. Calibrations

The ADC to PH calibrations were performed using spectra obtained with a ^{137}Cs source. The source was placed near the detectors, and the typical response of our neutron detectors to the 662-keV γ rays emitted from the ^{137}Cs source is shown in Fig. 2. The feature of interest in the distribution is the peak and decreasing slope starting near channel 900 and ending near channel 1300. The cesium edge location is defined to be the channel at which the number of counts reaches one-half of the maximum of the peak. The peak maximum and the cesium edge are indicated in the figure. The cesium edge location was the reference point used to carry out the calibration of each ADC spectrum. Data were collected using the ^{137}Cs source twice per day during the experiment.

A uniform ADC to PH calibration for each detector was useful for a few reasons. Calibrating the spectra places the PH parameter for each detector on the same absolute scale. This

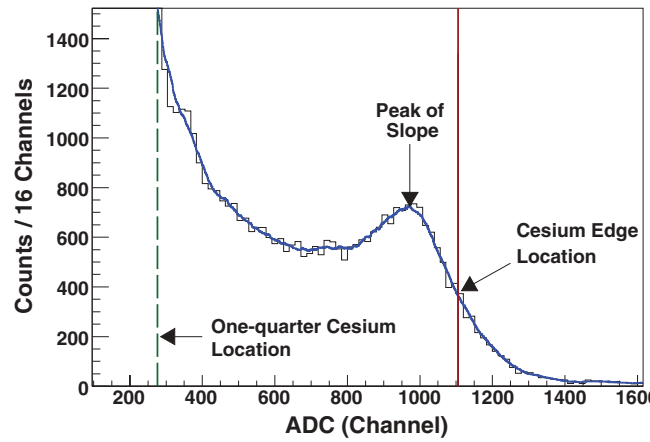

FIG. 2. (Color online) A typical ^{137}Cs source spectrum (black line histogram) from one of the Bicron liquid scintillator detectors. The source data were used to calibrate the ADC spectrum for each detector. The features of the spectrum indicated in the figure are described in Sec. III B. A smoothed version of the spectrum histogram is drawn on top of the original histogram (shown in blue online). The solid vertical line (shown in red online) indicates the one-cesium location, and the dashed vertical line (shown in green online) indicates the one-quarter-cesium location.

removes any small gain differences between the detectors, which allows a common software PH threshold to be used in the offline analysis. A common PH threshold ensures a common neutron detection efficiency as a function of neutron energy for the detectors, assuming there were no untracked gain shifts. In the offline analysis, the PH threshold was placed at *one-quarter cesium* (which is 0.25 times the channel value of the cesium edge) for the primary detectors, and the PH threshold was placed at *one cesium* (which is at the cesium edge location) for the beam intensity monitors. The one-quarter-cesium location is indicated by the dashed vertical line (shown in green online) in Fig. 2. Setting a one-quarter-cesium PH threshold implicitly sets a neutron energy threshold of $E_n = 1.5$ MeV, and thus we report no experimental data below this threshold. As we shall show in Sec. III G, the neutron detection efficiency is directly affected by the PH threshold, which in turn places a lower limit on the neutron energy.

Time-of-flight techniques were used to determine the kinetic energy of the neutrons detected in the experiment. A precise TDC calibration was needed since a continuum of neutron energies resulted from the three-body photodisintegration of ^{3}He. To accomplish the tasks of calibration of the TDC spectra and optimization of the event-selection cuts, we used an iterative approach for the placement of the cuts and fine tuning of the TDC to TOF calibration parameters. We discuss the TDC to TOF calibration here and delay the discussion of the cuts until Sec. III C.

The zero point of the TDC calibration, which indicates the beginning of an event, was found using the γ-flash spectra obtained from the detection of the γ rays scattered from a 12.7-cm-diameter aluminum rod placed at the center of the detector array. This rod provided a source of γ rays, and the TOF zero point was found by using the fact that it takes a γ ray d/c nanoseconds, where d is the flight path and c is the speed of light, to travel from the target to the detector. We performed short ($\sim$1 min) γ-flash runs between every production run using the aluminum rod to track any shifts in the TDC spectra.

The scale factor of the TDC module, measured in the ns/channel, was roughly determined using a delay line technique, where a TDC start was generated using a pulser and the delayed copy of the pulse was used as the TDC stop. Then, a fine tuning of the TDC scale factor was performed using the TOF results of a ^{2}H$(\gamma,n)^1$H GEANT4 simulation, which were compared to experimental TOF data taken with the ^2H_2O target placed at the center of the array instead of the aluminum rod. Comparing the experimental TOF data to the simulation TOF results required the PSD cut to be applied first. The fine tuning of the TDC scale factors was accomplished at one γ-ray energy, and it was verified that no changes to the scale factors were required at the other energies in order for the experimental TOF data to match the simulated TOF results.

C. Event-selection cuts

The correlations between the PH, PSD, and TOF parameters were exploited through the application of cuts on the recorded events. Each data run was replayed event by event and these cuts were applied to discard undesired data points. Both the experimental data and the data resulting from GEANT4 simulations were sorted in an identical manner.

In both the experiment and the simulations, neutrons and γ rays strike the detector and produce signals. A cut was placed on the data to discard γ-ray events, keeping the desired neutron events. The PSD properties of the neutron detectors were exploited to accomplish this task with the experimental data. The processing of the detector signals was carried out through the use of commercially available MPD-4 modules [13] manufactured by Mesytec. A larger PSD value from an MPD-4 module indicated a neutron event, while a smaller PSD value indicated a γ-ray event. A hardware PSD threshold was utilized to eliminate a large fraction of the γ-ray background events, but some events were allowed through. This deliberate placement of the hardware PSD threshold allowed us to optimize the final location of the PSD cut in the offline analysis software. PSD methods could not be used in the GEANT4 simulations since the detector pulse shapes were not simulated, and the particle identification cut was applied based on the name of the particle striking the detector, i.e., "neutron" or "gamma". This resulted in perfect γ-ray discrimination in the simulations.

We determined a PSD cut location for each detector by looking at its TOF versus PSD spectrum, where the TOF scale was determined using the calibration described in Sec. III B. In the TOF versus PSD spectra, such as the one shown in Fig. 3, the neutron events can be clearly identified and are well separated from both the random and time-correlated γ-ray events. The PSD cut for a single detector is indicated by the black line near PSD channel 1300 in the figure. Events to the right of the cut line and greater than 25 ns were kept.

The γ-flash peak is also indicated in Fig. 3. Events in this peak were unambiguously identified as γ rays by the measured time of flight, and these γ rays were Compton scattered into the detector by the walls of the aluminum target bottle. The rate of these γ-flash events was high enough to produce pileup in the MPD-4 modules, which led to a γ-flash event possessing a neutronlike PSD value. As is shown in Fig. 3, many γ-flash

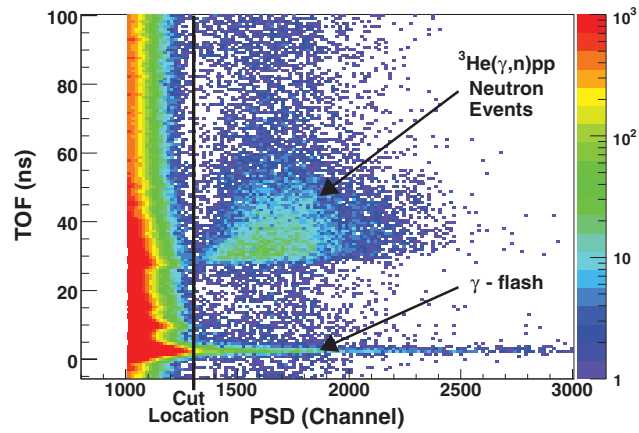

FIG. 3. (Color online) A TOF vs PSD spectrum for a single detector after the TDC to TOF calibration was performed. The neutron events are well separated from both the random and time-correlated γ-ray events. The PSD cut location is indicated by the solid black line near channel 1300.

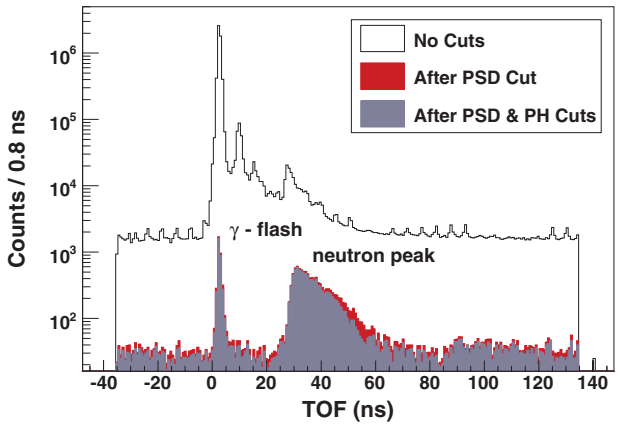

FIG. 4. (Color online) The effects of the event-selection cuts on the TOF spectrum of one of the primary neutron detectors. In the neutron peak, a larger TOF indicates a lower energy neutron.

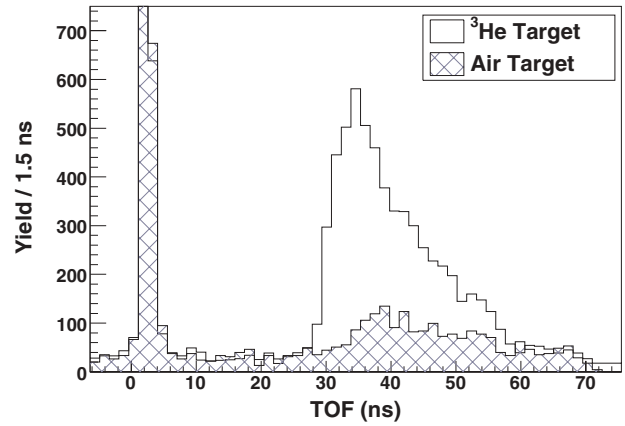

FIG. 5. (Color online) A comparison of the TOF yield spectra from the ^{3}He target and air target at $E_\gamma = 12.8$ MeV. The background (air) target was an aluminum target bottle identical to the ^{3}He target bottle filled only with air (no ^{3}He) at atmospheric pressure. See the discussion in Sec. III D for a description of the origin of the background events.

events had a PSD value larger than the majority of the neutron events from the ^{3}He$(\gamma,n)pp$ reaction. Of course, the γ-ray pileup is not a problem since the γ-flash events are easily distinguished from the neutrons via their time of flight.

A hardware threshold was set for each detector using a CFD at the beginning of the experiment. This threshold placed a lower limit on the pulse heights allowed and was used to suppress electronic noise and pulse pileup effects. The CFD threshold for each detector could be slightly different depending on gain differences between the detectors. Since the pulse height threshold directly affects the neutron detection efficiency, a pulse height cut was placed above the highest CFD threshold for the primary detectors and separately for the beam intensity monitor detectors (the PH threshold for the primary detectors was set to one-quarter cesium and to one cesium for the beam intensity monitor detectors). This was done to ensure that the efficiency of each detector was the same, given that there were no untracked gain shifts in the detectors. The PH threshold was determined after the ADC spectra for the neutron detectors were calibrated.

Figure 4 demonstrates the effects that the event-selection cuts have on the TOF spectra. The PSD cut discards the majority of the unwanted γ-ray background. The PH cut, applied after the PSD cut, has a small effect on the TOF spectrum because the CFD threshold was placed very close to the anticipated PH cut location (as discussed in Sec. III B) during the experimental setup. The largest effect of applying the PH cut is seen in the difference between the light-filled histogram (shown in gray online) and the dark-filled histogram (shown in red online) in the region between 40 and 60 ns. The events here, which were discarded as a result of introducing a PH threshold that is higher than the CFD threshold, are identified as lower energy neutrons by their location in the spectrum. Discarding neutron events by raising the PH threshold, of course, directly affects the efficiency as we will discuss in Sec. III G.

D. Background subtraction

Figure 5 plots the normalized TOF yields from both the ^{3}He target (plus bottle) against the normalized TOF yields from the background (air) target bottle at $E_\gamma = 12.8$ MeV. Both histograms were normalized to beam intensity and corrected for data acquisition (DAQ) dead time. The target bottles are made of the aluminum alloy 6082, which is approximately 95% ^{27}Al by weight. The neutron separation energy for ^{27}Al is 13.1 MeV and, thus, no neutron background was created from photonuclear interactions with ^{27}Al at this energy. The remaining 5% of the aluminum alloy 6082 contains small amounts of other elements, such as manganese, iron, copper, and zinc. The presence of these other elements in the gas bottle accounted for the neutron background underneath the ^{3}He$(\gamma,n)pp$ neutron peak. Some of the isotopes of these elements have neutron separation energies below 12.8 MeV and photoneutron cross sections in the 20–40 mb range at this energy. The target-related background seen in the figure was consistent with that produced by neutrons coming from photonuclear reactions with these isotopes.

At $E_\gamma = 13.5$ MeV, the γ-ray energy was above the neutron production threshold in ^{27}Al, but the energy of the outgoing neutrons produced by ^{27}Al was too low to produce a signal in the detector above the PH threshold. Thus, only a small increase in neutron background was observed due to the other elements present in the aluminum alloy 6082. The highest incident γ-ray energy used in the experiment, 14.7 MeV, is well above the neutron production threshold of ^{27}Al and, as a result, a large neutron peak was seen in the TOF spectra. However, the large background is present at lower neutron energies (or equivalently at larger TOFs), and the shape of the background is represented well by the air target yields at $E_\gamma = 14.7$ MeV.

The background (air target) TOF data were subtracted directly from the signal-plus-background (^{3}He target) TOF data to form the background-subtracted TOF yields. The background-subtracted TOF yields were then used to form the absolute differential cross section as a function of incoming γ-ray energy, outgoing neutron energy, and outgoing neutron angle.

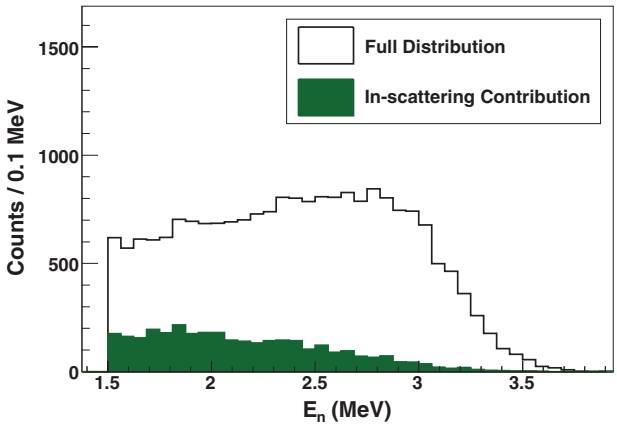

FIG. 6. (Color online) The full simulated distribution and the in-scattering contribution to that distribution using the Deltuva, Fonseca, and Sauer calculations [7] as the input cross section to the simulation. Note the suppressed zero on the horizontal scale.

E. Monte Carlo simulations

The Monte Carlo simulations were written using the GEANT4 toolkit. All of the physical objects shown in Fig. 1 were included in the GEANT4 world volume. All the volumes were needed to correctly reproduce the neutron in-scattering that will be discussed in Sec. III F. GEANT4 simulations were also used in calibrating the TDC spectra as we related in Sec. III B. As we will present in Sec. IV, the experimental data were compared to GEANT4 simulation results using both the calculations of Deltuva, Fonseca, and Sauer [7] and a phase-space calculation as the input cross section of the simulations.

F. Neutron in-scattering backgrounds

A neutron, which was not initially directed toward a detector, can be "in-scattered" into the detector by any volume near the detector, such as the walls of the target bottle, the aluminum plates of the target actuator, and adjacent detectors. These types

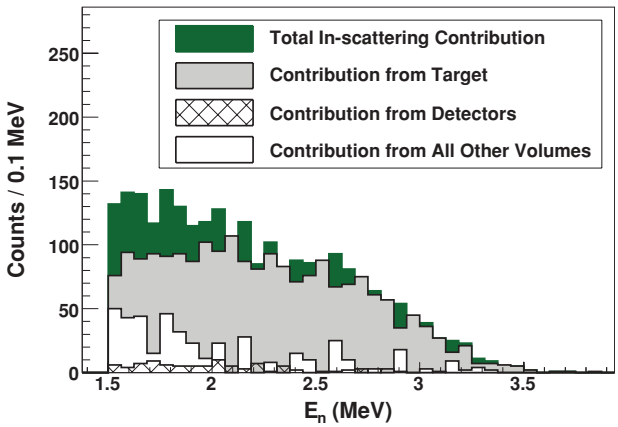

FIG. 7. (Color online) A breakdown of the in-scattering contribution shown in Fig. 6. Note the suppressed zero on the horizontal scale.

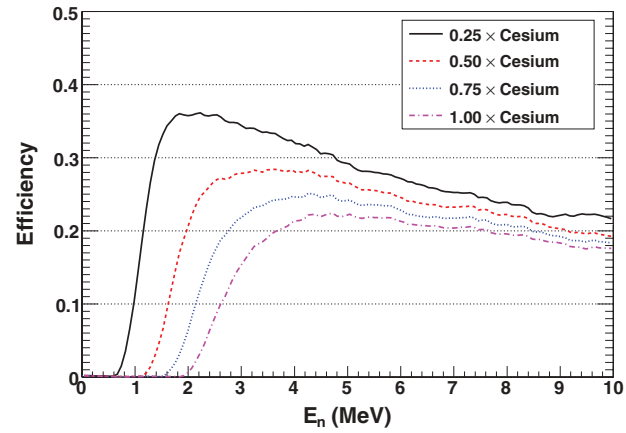

FIG. 8. (Color online) The dependence of the neutron detection efficiency on the PH threshold as calculated from GEANT4 simulation results for the liquid scintillator neutron detectors used in the experiment. A threshold of 0.25 × cesium and 1.00 × cesium was used for the primary and beam intensity monitor detectors, respectively.

of events occurred with the target-detector configuration used in the experiment, and investigations into the major sources of the in-scattering contribution were carried out using the GEANT4 simulations. Figure 6 shows, for one detector, the in-scattering contribution of the full simulated distribution using the Deltuva, Fonseca, and Sauer calculation [7] as the input. The in-scattering contribution is greatest at the lower neutron energies and decreases as the neutron energy is increased. A breakdown of the sources of in-scattered neutrons is shown in Fig. 7. This figure demonstrates that the majority of the in-scattering contribution is due to the target (including its walls and valve). At lower neutron energies, other volumes, such as aluminum plates and lead walls, contribute to the distribution. Scattering from adjacent detectors adds a small number of counts to the distribution.

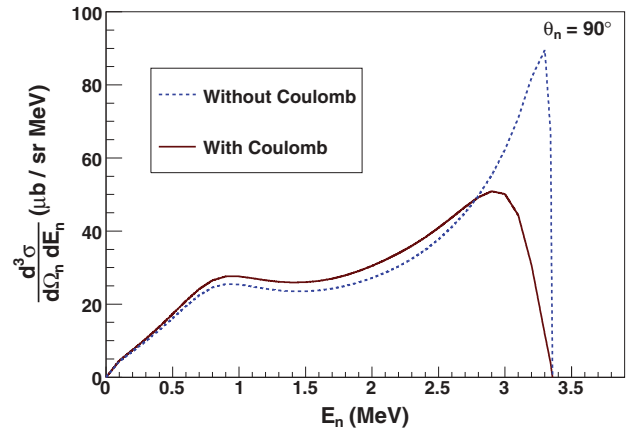

FIG. 9. (Color online) The theoretical calculation results for the ^{3}He$(\gamma,n)pp$ differential cross section at the incident γ-ray energy of 12.8 MeV and at the scattering angle of 90° showing the effect of including the Coulomb interaction in the final state.

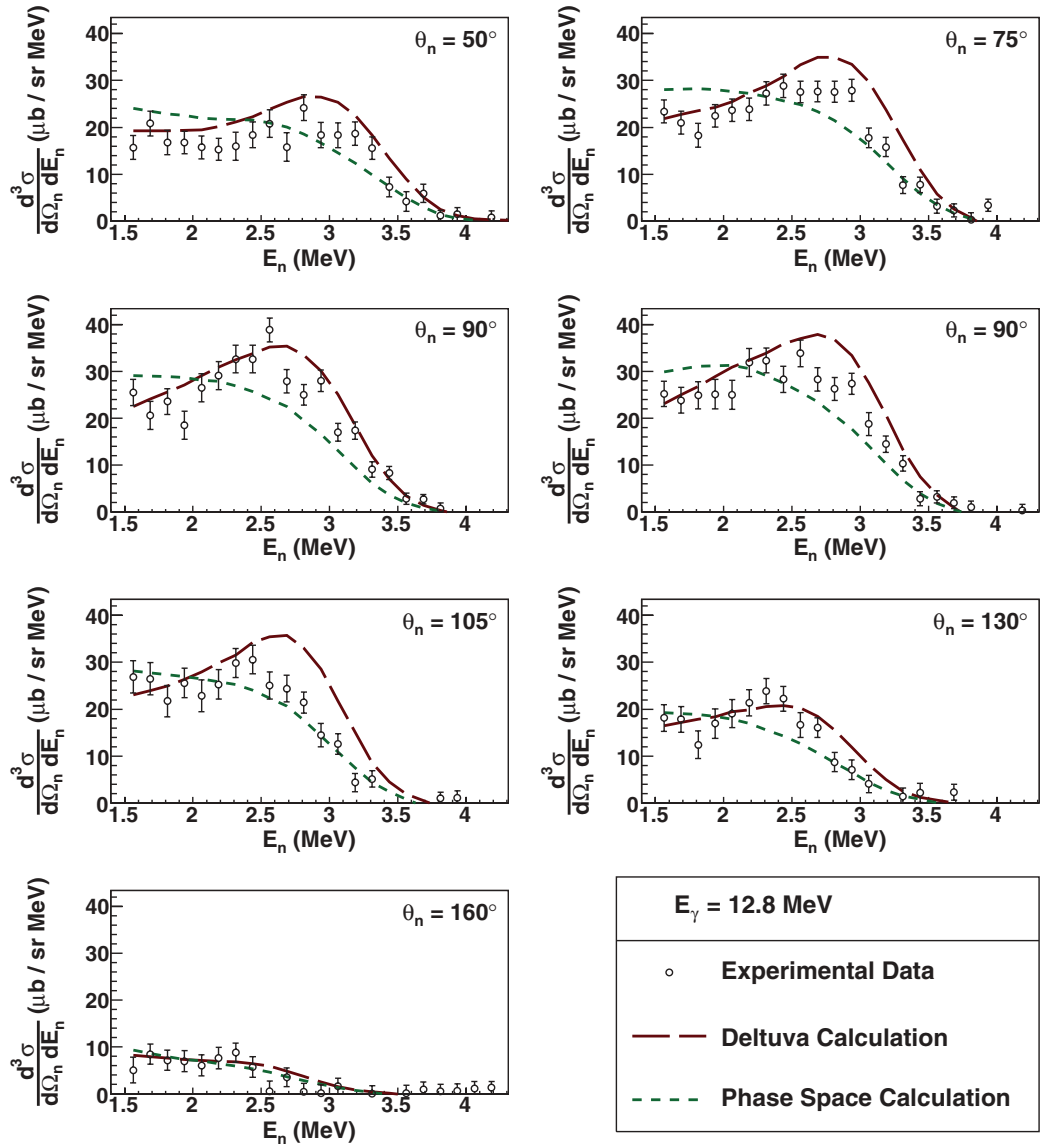

FIG. 10. (Color online) Experimental absolute differential cross sections at 12.8 MeV compared to simulation results using both the calculations provided by Deltuva [7] and phase-space calculations as the input cross sections.

G. Detector efficiency

Having an accurate knowledge of the neutron detection efficiency as a function of neutron energy of the Bicron liquid scintillator detectors was critical in determining the absolute differential cross sections. The efficiency was calculated using GEANT4 simulations that relied on light-output curves that were determined in previous measurements using these detectors. The measurements of the light-output response of the Bicron detectors were performed at the Physikalisch-Technische Bundesanstalt (PTB) in Braunschweig, Germany [14]. From the studies performed at PTB, light-yield curves were generated for protons, deuterons, alphas, beryllium nuclei, carbon nuclei, boron nuclei, and electrons. The light yield is given in units of MeVee (MeV electron equivalent) (one MeVee is the amount of light energy generated by an electron having a kinetic energy of 1 MeV). The neutron detection efficiency is dependent on the chosen pulse height threshold as we have mentioned throughout this paper, and Fig. 8 shows the dependence of the neutron detection efficiency on pulse height threshold (relative to the cesium edge location) as calculated for the Bicron liquid scintillator neutron detectors used in the experiment.

IV. RESULTS COMPARED TO THEORY

A. Theory

Deltuva, Fonseca, and Sauer [5] have made progress in solving three- and four-particle scattering problems including a full treatment of the Coulomb interaction in the final state. The calculations are made in the framework of integral scattering equations in momentum space. The calculations use the methods of screening and renormalization and are implemented in a novel way, allowing the use of a realistic

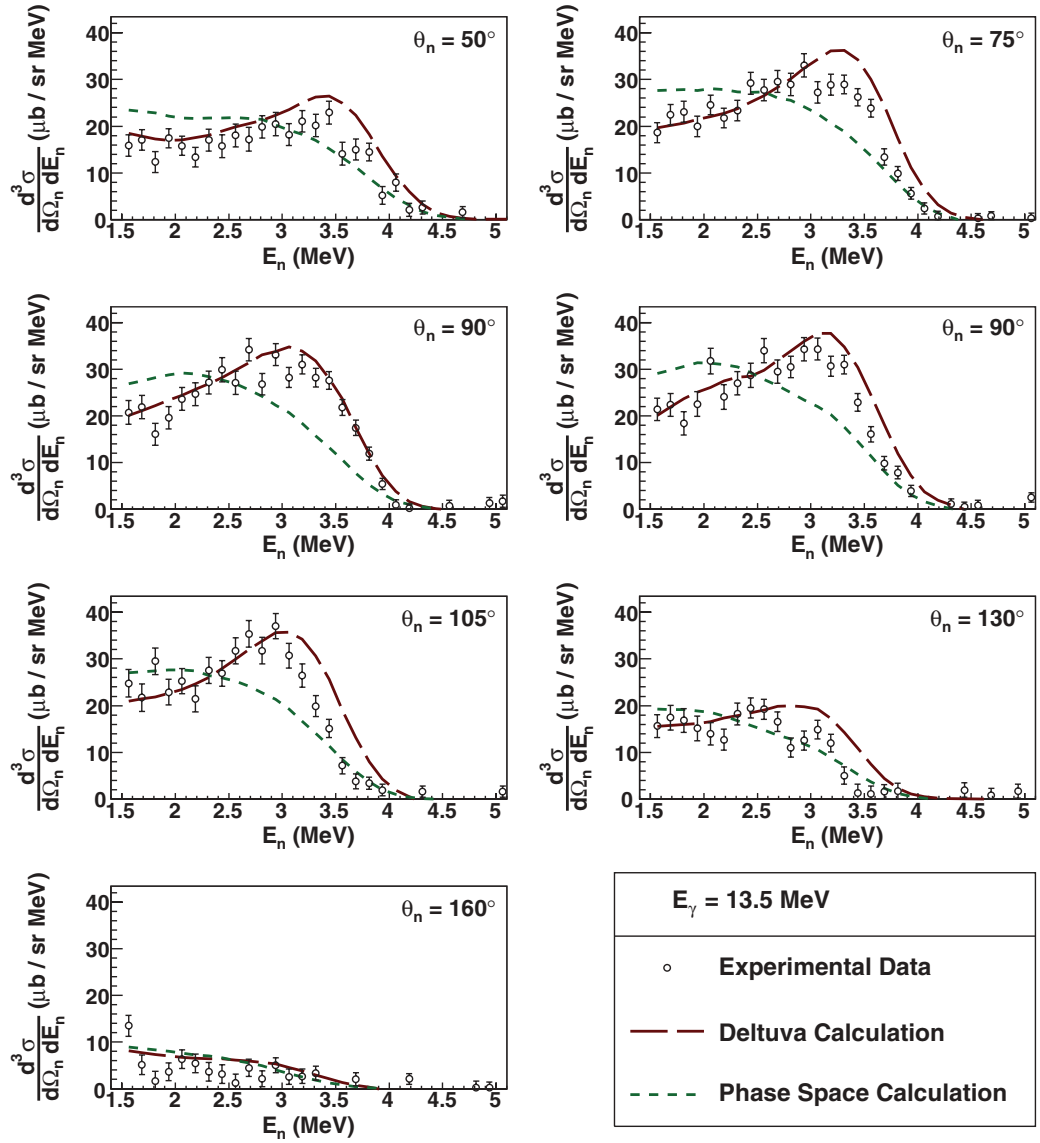

FIG. 11. (Color online) Experimental absolute differential cross sections at 13.5 MeV compared to simulation results using both the calculations provided by Deltuva [7] and phase-space calculations as the input cross sections.

potential model along with a full treatment of the Coulomb potential.

The results for the three-body scattering calculations for the ^{3}He$(\gamma,n)pp$ reaction at the incident γ-ray energies of 12.8, 13.5, and 14.7 MeV were provided by Deltuva [7]. Figure 9 shows the theoretical predictions for the ^{3}He$(\gamma,n)pp$ differential cross section at the energy of 12.8 MeV and at the scattering angle of 90°. The dashed curve (shown in blue online) in the figure is the result of the scattering calculation without the inclusion of the Coulomb interaction between the protons in the final state. The solid curve (shown in red online) is the result when the Coulomb interaction is included. The effect, at each scattering angle, of including the Coulomb potential in the calculations is to reduce the peak cross section near $E_n^{\max}$ by approximately 40% in magnitude and shift the peak location down in energy.

B. Cross-section results

The experimental absolute differential-cross-section data at each γ-ray energy are shown compared to two simulated distributions at each scattering angle in Figs. 10, 11, and 12. The long-dashed curves (shown in red online) in the figures are the GEANT4 simulation results using the calculations provided by Deltuva as the cross-section input to the simulation. The short-dashed curves (shown in green online) are phase-space simulation results. Recall from Sec. I that Gorbunov [2] found agreement between the experimental neutron energy distributions at $E_\gamma = 8$–12 MeV and a phase-space-only neutron energy distribution. It is interesting to also compare the neutron energy distributions from the current experiment with phase-space distributions. It is important to note that the phase-space calculations do not provide a prediction for either the absolute scale of the cross section or its angular dependence, only the

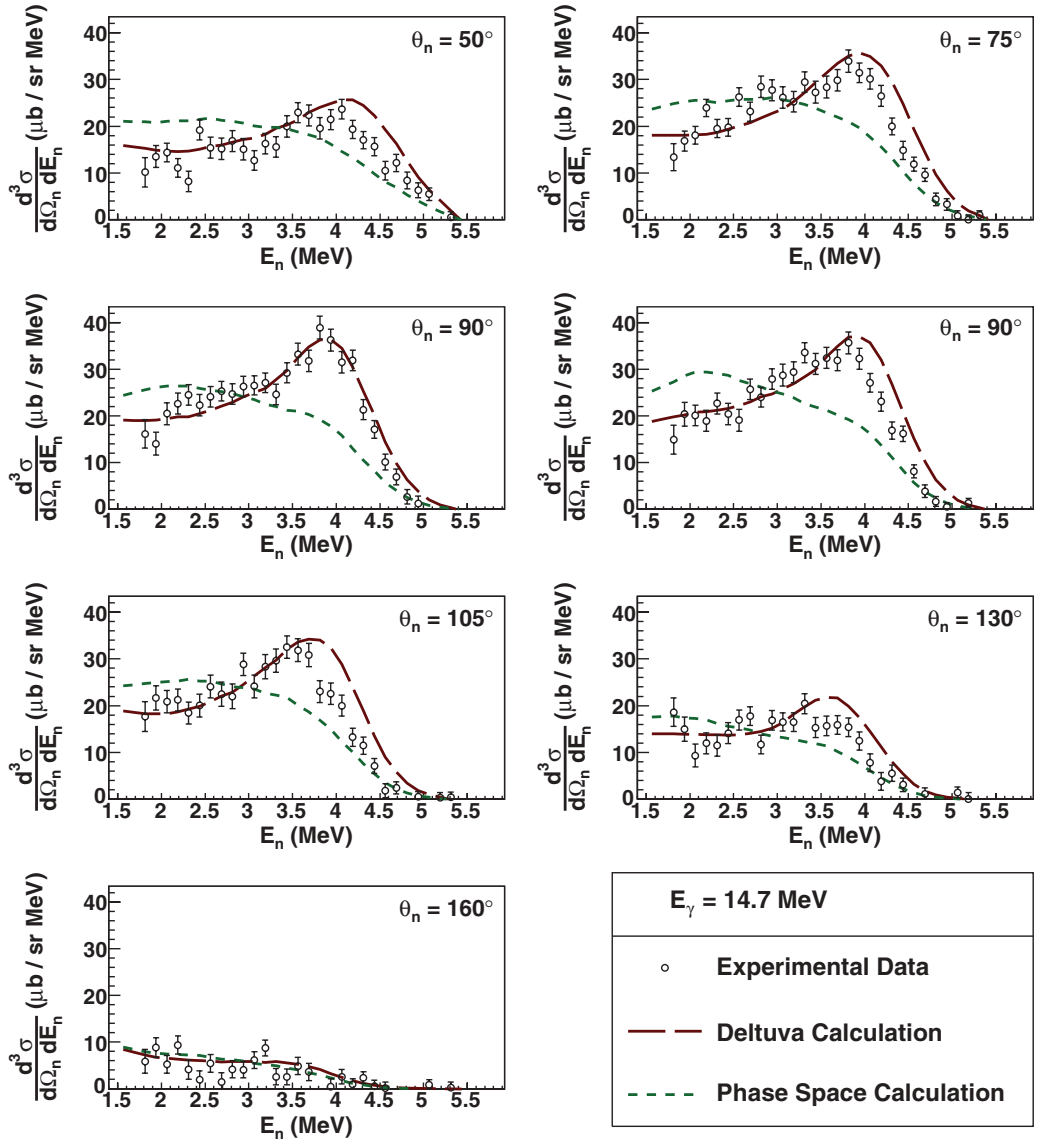

FIG. 12. (Color online) Experimental absolute differential cross sections at 14.7 MeV compared to simulation results using both the calculations provided by Deltuva [7] and phase-space calculations as the input cross sections.

shape of the neutron distribution at a given neutron scattering angle. To compare the phase-space simulation results to the theoretical prediction, the angular distribution was specified to be of the form $A\sin^2(\theta_n^{\rm cm}) + \delta$, with $A = \frac{3}{8\pi}(1 - 0.15)$ and $\delta = \frac{1}{4\pi}(0.15)$, and the total number of events thrown into 4π steradians was normalized to the Deltuva total cross section at the given γ-ray energy.

As can be seen in the figures, the experimental cross sections are in excellent agreement with the theoretical prediction in absolute scale. (Note again that the phase-space calculations were normalized to have the same total area as the theoretical total cross section.) In addition, the shapes of the neutron distributions at each γ-ray energy and at each scattering angle are reasonably consistent with the theoretical calculations of Deltuva, Fonseca, and Sauer that include the Coulomb interaction between the protons in the final state. The key feature of the predicted neutron energy distributions at a particular scattering angle is the peaking of the cross section near 90% of $E_n^{\rm max}$. (The physical origin of this peak is discussed in the paper by Barbour and Phillips [3].) At each γ-ray energy and scattering angle, except for $\theta_n^{\rm lab} = 160^\circ$, the measured cross-section data show the same peaking near the maximum neutron energy. The exact location of the peak is well reproduced, although the data at 75° and 105° indicate a value that is somewhat lower than predicted. By contrast, the phase-space neutron energy distributions do not show a peaking near the maximum neutron energy, and are in disagreement with the majority of the experimental data at all three energies.

V. SYSTEMATIC UNCERTAINTIES

The total systematic uncertainty in the extraction of the absolute cross sections was estimated to be less than ±6%. This

TABLE I. Summary of the sources of systematic uncertainty.

Source	Value (%)
^{2}H(γ,n)^{1}H cross section	3.6
Detector efficiencies	2.8
Target lengths	1.2
^{3}He target pressure	2.0
Detector solid angles	1.4
Pulse-shape discrimination cut	1.0
Detector gain determination	1.5
Background subtraction	1.0
Total (added in quadrature)	5.7

total systematic uncertainty was determined by combining the individual sources of error in quadrature. Table I provides a summary of the sources of systematic error.

VI. SUMMARY AND CONCLUSIONS

Absolute cross sections of the ^{3}He(γ,n)pp reaction as a function of the outgoing neutron energy and scattering angle were measured at the incident γ-ray energies of 12.8, 13.5, and 14.7 MeV. This experiment is the first to provide angular and energy distributions of the outgoing neutrons at well-defined energies. Previously, only distributions averaged over the incident γ-ray bins of 8–12 and 12–16 MeV existed.

The data at all energies were compared to phase-space calculations and the state-of-the-art three-body calculations provided by Deltuva [7], which include the Coulomb interaction between the protons in the final state. The experimental differential cross sections agree with the calculations of Deltuva, Fonseca, and Sauer [7], both in the shape of the outgoing neutron energy distributions and the absolute scale. This agreement in absolute values is in contrast to the results of Naito *et al.* [4], which are discrepant with theory by about a factor of 3 at the slightly lower incident γ-ray energy of 10.2 MeV.

ACKNOWLEDGMENTS

The authors thank A. Deltuva for providing calculations and for helpful discussions. This work was supported in part by the US Department of Energy, Office of Nuclear Physics, under Grant No. DE-FG02-97ER41033.

[1] A. N. Gorbunov and A. T. Varfolomeev, Phys. Letts. **5**, 149 (1963); B. L. Berman, L. J. Koester Jr., and J. H. Smith, Phys. Rev. **133**, B117 (1964), and references therein.
[2] V. N. Fetisov, A. N. Gorbunov, and A. T. Varfolomeev, Nucl. Phys. **71**, 305 (1965); H. M. Gerstenberg and J. S. O'Connell, Phys. Rev. **144**, 834 (1966); A. N. Gorbunov, in *Photonuclear and Photomesic Processes*, edited by D. V. Skobel'tsyn (Consultants Bureau, New York, 1974), Vol. 71, pp. 1–117; B. L. Berman, S. C. Fultz, and P. F. Yergin, Phys. Rev. C **10**, 2221 (1974); D. D. Faul, B. L. Berman, P. Meyer, and D. L. Olson, *ibid.* **24**, 849 (1981).
[3] J. C. Gunn and J. Irving, Philos. Mag. Ser. **42**, 1353 (1951); I. M. Barbour and A. C. Phillips, Phys. Rev. C **1**, 165 (1970); B. F. Gibson and D. R. Lehman, *ibid.* **13**, 477 (1976).
[4] S. Naito *et al.*, Phys. Rev. C **73**, 034003 (2006).
[5] A. Deltuva, A. C. Fonseca, and P. U. Sauer, Annu. Rev. Nucl. Part. Sci. **58**, 27 (2008).
[6] H. R. Weller *et al.*, Prog. Part. Nucl. Phys. **62**, 257 (2009).
[7] A. Deltuva, A. C. Fonseca, and P. U. Sauer, Phys. Rev. C **72**, 054004 (2005), and private communication.
[8] Chemgas, Certificate of quality No. 20031644 [http://www.chemgas.com].
[9] Y. Birenbaum, S. Kahane, and R. Moreh, Phys. Rev. C **32**, 1825 (1985); R. Bernabei *et al.*, Phys. Rev. Lett. **57**, 1542 (1986).
[10] H. Arenhövel, A. Fix, and M. Schwamb, Phys. Rev. Lett. **93**, 202301 (2004); M. Schwamb and H. Arenhövel, Nucl. Phys. A **696**, 556 (2001); **690**, 682 (2001).
[11] M. A. Blackston, Ph.D. thesis, Duke University, 2007.
[12] J. Allison *et al.*, IEEE Trans. Nucl. Sci. **53**, 270 (2006).
[13] A. Ruben *et al.*, Nuclear Science Symposium Conference Record, 2007. NSS '07. IEEE, p. 681; Mesytec GmbH & Co. KG [http://www.mesytec.com/].
[14] D. E. G. Trotter *et al.*, Nucl. Instrum. Methods Phys. Res., Sect. A **599**, 234 (2009).